American Society of Mechanical Engineers

ASME Accepted Manuscript Repository

Aerodynamics of a Convex Bump on a Ground-effect Diffuser

O. H. Ehirim
Ph.D. Research Student
o.ehirim@cranfield.ac.uk

K. Knowles
Professor and Head of Group
k.knowles@cranfield.ac.uk

A. J. Saddington[*]
Senior Lecturer
a.j.saddington@cranfield.ac.uk

M. V. Finnis
Principal Research Fellow
m.v.finnis@cranfield.ac.uk

Aeromechanical Systems Group,
Cranfield University, Shrivenham, SN6 8LA, UK

Abstract: A ground-effect diffuser is an upward-sloping section of the underbody of a racing car that enhances aerodynamic performance by increasing the downforce, thus improving tire grip. The downforce generated by a diffuser can be increased by geometric modifications that facilitate passive flow control. Here we modified a bluff body equipped with a 17° diffuser ramp surface (the baseline/plane diffuser) to introduce a convex bump near the end of the ramp surface. The flow features, force and surface pressure measurements determined in wind-tunnel experiments agreed with previous studies but the bump favorably altered the overall diffuser pressure recovery curve by increasing the flow velocity near the diffuser exit. This resulted in a static pressure drop near the diffuser exit followed by an increase to freestream static pressure, thus increasing the downforce across most of the ride heights we tested. We observed a maximum 4.9% increase in downforce when the modified diffuser was compared to the plane diffuser. The downforce increment declined as the ride height was gradually reduced to the low-downforce diffuser flow regime.

Keywords: aerodynamics, ground-effect diffuser, convex-surface, pressure-recovery, downforce

[*] Corresponding author address: Aeromechanical Systems Group,
Centre for Defence Engineering, Cranfield University,
Defence Academy of the United Kingdom, Shrivenham, SN6 8LA, UK

1. INTRODUCTION

The ground-effect diffuser is a major aerodynamic device fixed to the aft underbody of racing cars, which comprises a single diverging ramp that produces downforce via a velocity/pressure flow relationship. When air travels through the diverging area it produces downforce by inducing pressure recovery from the peak velocity and peak suction flow at the diffuser inlet to the low-velocity and low-suction flow at its exit [1, 2]. The ground-effect diffuser produces ~40% of total downforce for a Formula One car, enhancing aerodynamic stability and cornering performance [3]. In close proximity to the road surface (or a solid ground plane), diffuser performance becomes sensitive to instabilities in the ground-effect flow regimes [4].

Previous experimental investigations have considered the flow features and aerodynamic performance of ground-effect diffusers. A longitudinal vortex pair forms along the edges of the diffuser ramp surface and the enhanced velocity inflow created by the vortex pair reduces the static pressure and prevents flow separation within the diffuser [5, 6]. Furthermore, at a given diffuser length, a given pressure recovery gradient that determines downforce levels can be achieved with a smaller diffuser area ratio under moving ground conditions compared to fixed ground conditions [7, 8]. This has been attributed to the flow blockage effects on the fixed ground due to boundary layer growth [7, 8].

Senior et al. [9-11] found that flow behavior and diffuser downforce are dependent on diffuser ride height, which regulates the constrained underbody airflow entering the diffuser. Downforce was shown to increase at lower ride heights until a maximum downforce is reached, and further ride-height reduction causes downforce loss [11]. Likewise, the initial reduction in ride height increased the flow velocity of the constrained airflow, which increased the size and strength of the longitudinal vortex pair [5]. However, when the ride height was reduced further, vortex breakdown occurred due to the diffuser inflow being dominated by the underbody boundary layer. Additionally, at the maximum-downforce ride height, the separation point of the diffuser flow from the ramp surface was found to depend upon the diffuser angle, which determines the flow-turning effect at the diffuser inlet [12]. At low angles, flow separation on the diffuser ramp was delayed (5°) or formed downstream of the diffuser inlet (10°), whereas at high angles (15°, 17° and 20°) a separation bubble formed close to the diffuser inlet. However, fixed-ground wind tunnel investigations have shown that the separation bubble initially appears when $\theta > 13°$ [13, 14]. Numerical analysis [15, 16] and corresponding empirical experiments have also

2

highlighted the pressure/velocity relationship and pressure recovery attributes of the ground-effect diffuser.

These previous studies have provided a fundamental understanding of the downforce-generating flow regimes and flow features within the ground-effect diffuser. In the present work we investigated a passive flow-control method that enhances the downforce generated by a diffuser. Passive flow-control methods are typically geometrical modifications of a high-lifting surface. Various alterations applied on aerodynamic surfaces have been explained by Gad-el-Hak [17] to alter boundary layer flow by doing any of the following: delay flow separation; add energy to boundary layer flow; or control boundary layer flow instabilities by mixing sub-layers within the boundary layer. Common passive flow control devices are vortex generators, which exist in various shapes and have been found to induce streamwise vortices that energize boundary layer flow on aerodynamic surfaces in ground-effect [18-20]. On a diffuser in ground effect, Jowsey & Passmore [13] and Jowsey [14] discovered that the addition of fences to split the diverging area of the diffuser into multiple flow channels enhanced downforce production due to the creation of secondary longitudinal vortices by the inner fences, from the cross-flow of the primary vortices along the edges of the outer fences of the diffuser. However, the fundamental principle by which the diffuser generates downforce is its pressure recovery performance [7, 8], as shown in Figure 1a, where static pressure rises from the peak suction at the diffuser inlet (C_{P1}) to the higher freestream pressure at the diffuser exit (C_{P2}). Downforce can be increased by altering the pressure recovery gradient. A static pressure drop (C_{P3}) downstream of the diffuser inlet delays pressure recovery to the higher freestream pressure at its exit as illustrated in Figure 1b. Consequently, the downforce increases due to the lower average static pressure caused by the pressure recovery delay. Such delays require a corresponding change in the streamwise flow velocity due to the velocity/pressure relationship of the diffuser flow. Hence, increasing the flow velocity close to the diffuser exit induces a static pressure drop that results in a second stage of pressure recovery within the pressure recovery curve [21].

Second-stage pressure recovery, as presented in Figure 1b, requires the application of flow-curvature effects to increase the streamwise flow velocity close to the diffuser exit. The curvature in the form of a convex surface on the portion of the diffuser ramp towards the diffuser exit increases the velocity of the diffusing flow traveling towards the diffuser exit. Similar to the curvature of the suction surface of an airfoil, the increase in flow velocity induced by the surface

creates a pressure gradient by entraining airflow onto the surface (flow attachment). The occurrence in turn induces the second pressure drop across the diffuser pressure distribution. Therefore, modifying the shape of the smooth diffuser ramp surface by including a convex bump at the end of the ramp surface can enhance suction, thus increasing the overall downforce generated by the diffuser. Other flow characteristics that can be beneficial in keeping overall profile drag induced by the bump low, is the reduction in wall friction, turbulence intensity and shear stress that all accompany the pressure drop induced by wall-bounded flows over convex surfaces [22-25]. Here we applied the convex bump as a passive flow control technique to a diffuser-equipped bluff body, and determined the impact in terms of downforce and drag measurements, as well as flow features and behavior captured by static pressure distribution and flow visualization on the diffuser ramp surface.
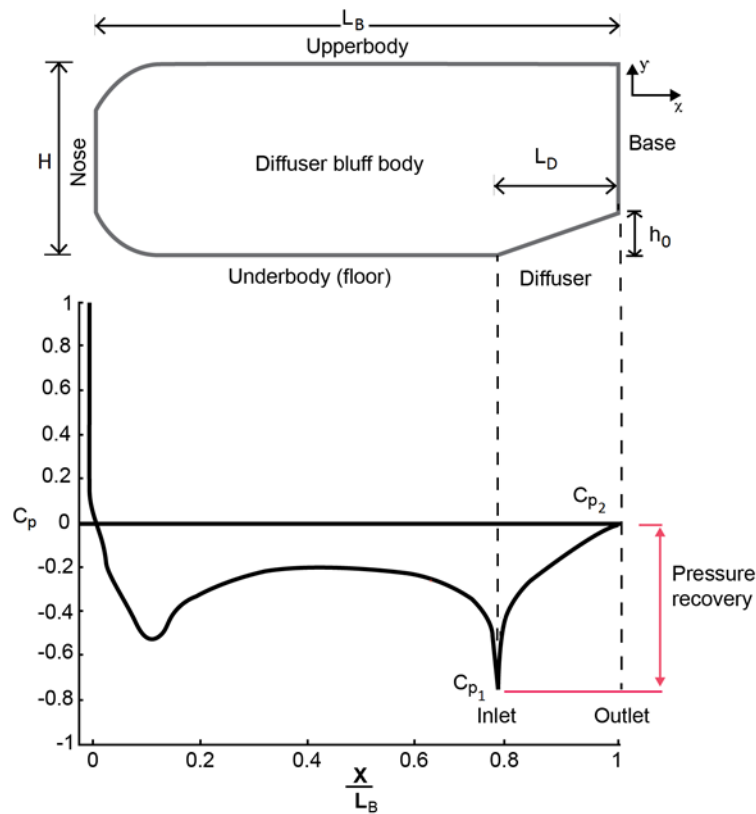

Fig 1a: The centerline underbody surface pressure behavior of a diffuser bluff body, highlighting the single-stage pressure recovery at the diffuser section with no flow control [21]
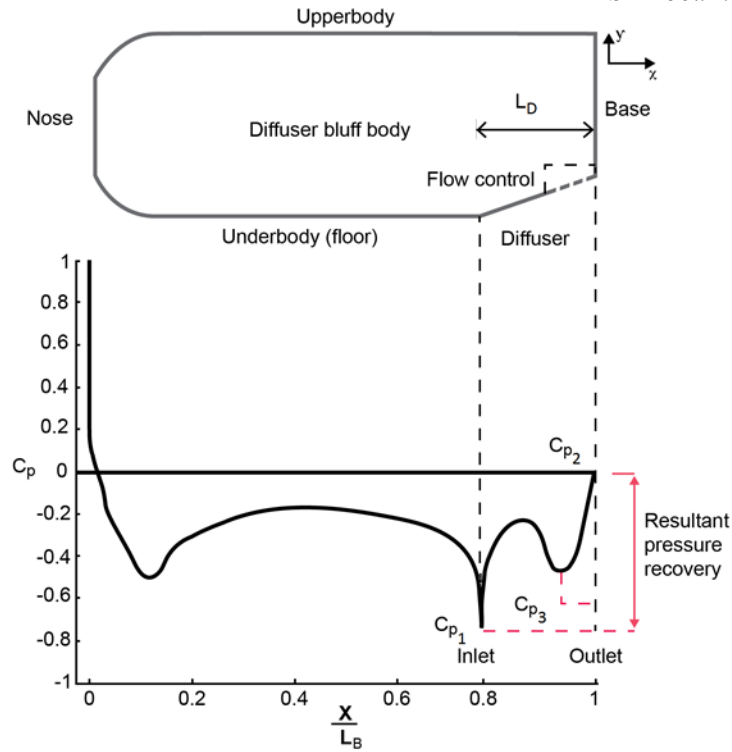
Fig 1b: The centerline underbody surface pressure behavior of the diffuser bluff body highlighting the two-stage pressure recovery at the diffuser section using flow control [21]

2. EXPERIMENTAL SETUP

2.1 Wind Tunnel Facility

All experiments were conducted in Cranfield University's closed-return, 3/4 open-jet "DS Houghton" wind tunnel, which has a nozzle $1.66\,m$ in height by $2.74\,m$ in width and an open test section $4.33\,m$ in length [26]. The use of the open test section negates the need for blockage effect corrections. The facility has a rolling-road ground simulation including a suction system for boundary layer removal. The latter enables the wind tunnel to reach a minimum of 98.4% total pressure $2\,mm$ above the belt. Freestream turbulence intensity within the test section is ~0.3%. The experiments were carried out at a rolling-road speed of $20\,m/s$ with the same freestream velocity ($U_\infty = 20\,m/s$), which equates to a Reynolds number of $Re = 1.8 \times 10^6$ based on bluff-body length.

2.2 Experimental Model

The experimental model comprised a bluff body equipped with a 17° diffuser ramp (plane diffuser, Figure 2a), which was modified by including a convex bump at the end of the ramp surface for passive flow control (modified diffuser, Figure 2b). The model was constructed from aluminum and SikaBlock polyurethane, and was mounted on an airfoil-shaped strut as shown in

5

Figure 2c. The bluff body was $0.326\,m$ high x $0.314\,m$ wide x $1.315\,m$ long, the same dimensions as used in previous investigations [11]. The body also included a pair of $0.005\,m$ thick end-plates on each side of the diffuser ramp. The convex bump was an arc with a length of $0.092\,m$, a height of $0.0056\,m$ and a span of $0.304\,m$. The bump was positioned across the diffuser span and formed part of the ramp surface close to the diffuser exit. The coordinate system for experimental measurements was placed at the end of the bluff body's nose section. The ride height h was defined as the distance between the underbody surface and the moving ground surface of the wind tunnel.
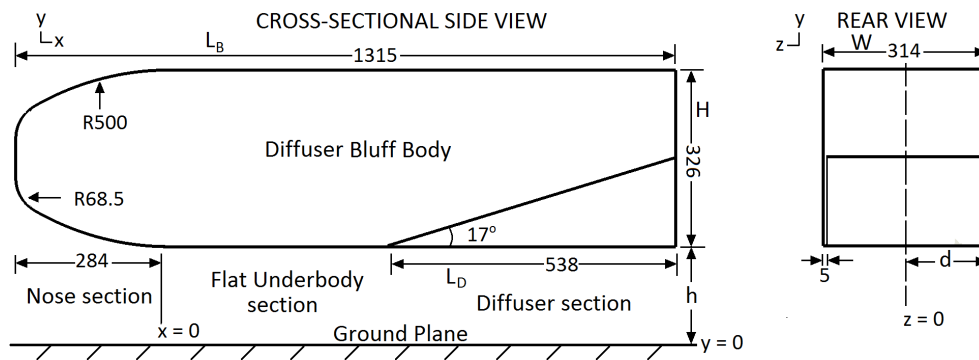
Fig 2a: Schematics of midplane cross-sectional and rear views of the baseline diffuser, a 17° plane diffuser ramp on a bluff body (dimensions in mm)
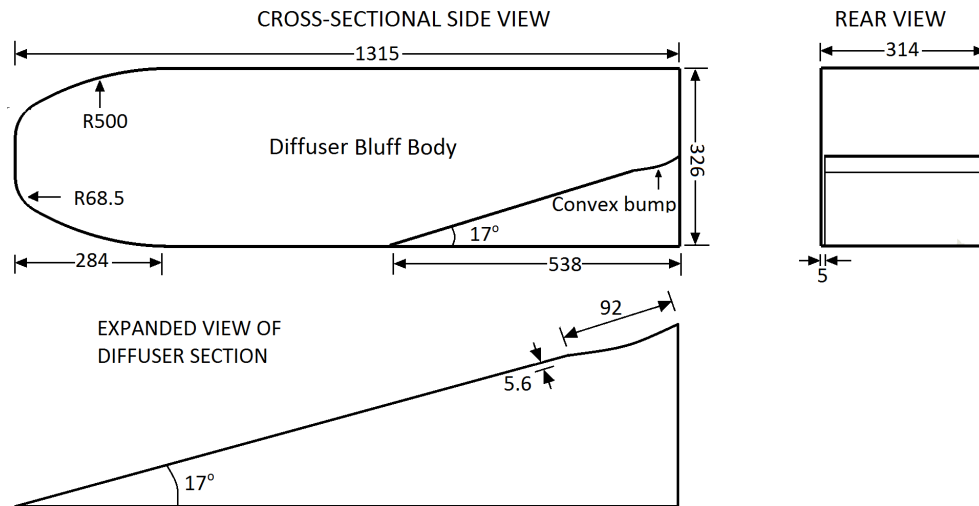
Fig. 2b: Schematics of midplane cross-sectional and rear views of the modified diffuser, a 17° diffuser ramp modified by including a convex bump (dimensions in mm)
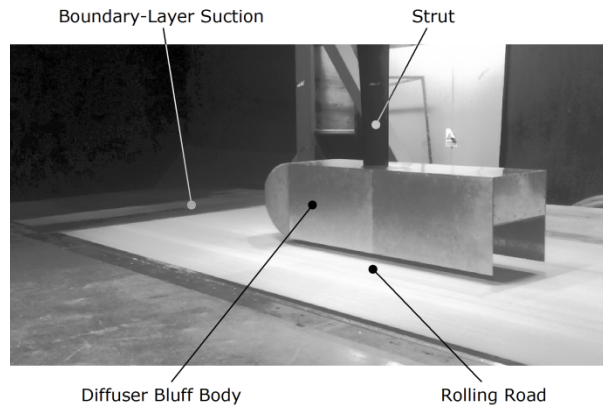
Fig. 2c: The experimental plane-diffuser bluff body model mounted on the overhead strut in the wind tunnel

2.3 Experimental Methods

Measurements were taken at 35 different ride heights ($120 \ mm$ to $10 \ mm$) and were non-dimensionalized at $h/d = 0.764$ to 0.064, where d is the half-width of the bluff body. Time-averaged downforce and drag values were measured using a six-component internal force balance. The coefficients of downforce, $-C_L$, and drag, C_D, were computed taking into account the variation of air density caused by changes in freestream pressure and temperature during the experiments. Seventy-one pressure taps distributed on the flat underbody and diffuser ramp surfaces were used to measure surface pressures, including 11 and 12 taps positioned in a line along the centerline of the flat underbody and diffuser ramp surfaces of the body, respectively, and 40 taps distributed equally transversally across the ramp surface in four rows ($x/d = 3.63, 4.10, 5.02$ and 5.95) with a fifth row ($x/d = 6.29$) of eight taps situated along the transverse mid-line of the convex bump's surface (Fig. 3). The flow visualization tests were conducted on the diffuser ramp surface using a paint-based mixture of fluorescent pigment, oleic acid and paraffin.

Error analysis was conducted to determine the total error, comprising the repeatability errors, measurement errors and stochastic errors. Repeatability was assessed by conducting non-consecutive test runs. Lift, drag and surface pressure coefficients were repeatable to ± 0.00010, ± 0.00024, and ± 0.003 respectively. Based upon the calibration of the force balance the measurement errors in lift and drag were $\pm 0.016\%$, $\pm 0.078\%$ of full-scale respectively. The model ride height was measured, using a drop height gauge, to an accuracy of ± 0.02 mm, and pitch and yaw were set to within $\pm 0.04°$ and $\pm 0.05°$ respectively. The measurement error in the dynamic pressure was $\pm 0.25\%$ and in the surface pressures was $\pm 0.20\%$; both relative to full-scale. The total uncertainties for the force and surface pressure coefficients were dependent upon a

combination of the uncertainties associated with the experiment as a whole, i.e. model ride height, pitch, yaw, dynamic pressure, force, and surface pressure.
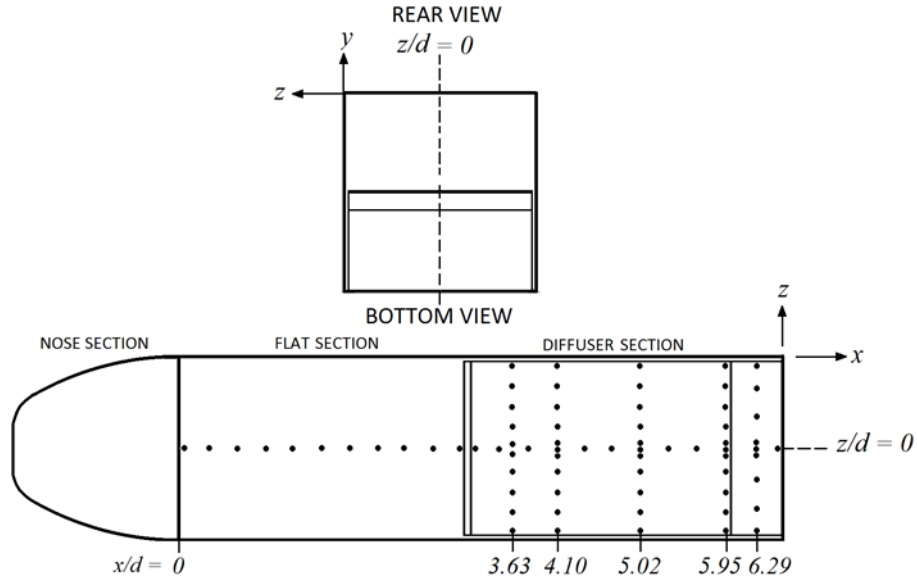

Fig. 3: Distribution of pressure taps on the bluff body lower surface

The total uncertainties were calculated using the root-mean-square method described by Abernathy et al. [27] and Moffat [28] and were determined, using a 95% confidence level, to be ±0.0025, ±0.0032, and ±0.057 for the lift, drag, and pressure coefficients respectively. Error bars have not been included in the subsequent plots as they are smaller than the symbols used.

3. ANALYSIS

3.1 Downforce, Drag and Aerodynamic Performance Analysis

The force measurements from the highest to the lowest ride heights within the tested range indicated the existence of four distinct diffuser flow regimes, which are shown as regimes 'A' to 'D' on the force curves in Figure 4. The boundaries between the flow regimes were determined by comparing the force plots with flow visualization from investigations using computational fluid dynamics [21]. The boundaries between regimes 'A' & 'B' and between 'C' & 'D' correspond to the points of inflection on the force curves while the boundary between regimes 'B' and 'C' is at the point of maximum force. Regime 'A' is classified as the force-enhancement regime, where the diffuser flow is reasonably symmetrical with the presence of a pair of longitudinal vortices. Regime 'B' is the maximum force regime, characterized by increased inlet suction and vortex pair size. Regime 'C' is denoted as the force-reduction regime, where the diffuser flow becomes

asymmetrical. Finally, regime 'D' is classified here as the low-downforce regime, where the asymmetrical flow is increasingly dominated by flow recirculation.
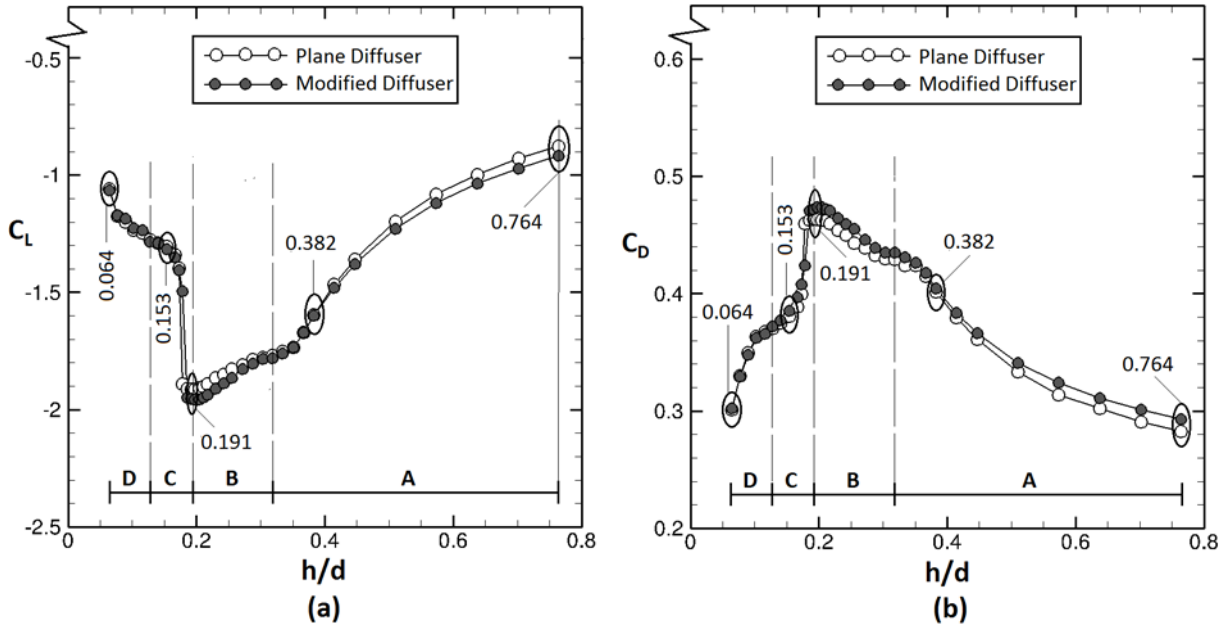

Fig. 4: Force coefficients across the range of ride heights investigated for the plane and modified diffusers: (a) C_L (b) C_D , showing the different flow regimes 'A', 'B', 'C' and 'D'

The C_L[1] and C_D plots in Figure 4 show that regime 'A' starts from the highest ride height of $h/d = 0.764$ and ends at $h/d = 0.318$. Within this sub-range of ride heights, downforce and drag increased gradually for both the plane and modified diffusers. The C_L value of the modified diffuser at $h/d = 0.764$ was 4.9% higher than that of the plane diffuser. Meanwhile, the C_D value of the modified diffuser at $h/d = 0.764$ was 3.54% higher than that of the plane diffuser. At $h/d = 0.318$, the modified diffuser increased C_L and C_D over the plane diffuser by 0.73% and 1.17% respectively.

Regime 'B' of the force measurements occurred between the ride heights of $h/d = 0.318$ and 0.191. Although downforce and drag increased in regime 'B' following a further decrease in the ride height, a change in the slope of the force curve indicated a change in the diffuser flow behavior. Regime 'C', which occurred between $h/d = 0.191$ and 0.127 features an abrupt reduction in C_L and C_D indicating another change in the diffuser flow physics. Downforce and drag continued to decline in regime 'D', but the decrease was smaller than in regime 'C' due to the low downforce in regime 'D'. Regime 'D' covers the ride height range from $h/d = 0.127$ to the lowest tested value of $h/d = 0.064$.

---

[1] Throughout this paper, C_L is positive upwards, with a negative value representing downforce.

Figure 5 shows the percentage change in C_L and C_D as ride height is changed. The largest increase in downforce occurs at $h/d = 0.764$ and gradually reduces to approximately zero at $h/d = 0.350$. In Regime 'B' the modified diffuser again shows an increase in downforce over the plain design. The large negative change in downforce seen at $h/d = 0.178$ is a consequence of the rapid change in C_L at this ride height. The changes in downforce are accompanied by similar changes in drag, i.e. an increase in downforce results in an increase in drag. In Figure 6, the lift-to-drag ratio, and its percentage change, across the range of ride heights indicates that the modified diffuser performs better, based on this metric, in Regimes 'A' and 'B'. However, although lift-to-drag ratio is a common indictor of aerodynamic performance, racing cars tend to operate in one of two general setups: a high downforce, high drag mode; a low downforce, low drag mode. The former being of more interest in the current study. In this respect, the modified diffuser can offer a higher level of downforce whilst maintaining an equivalent lift-to-drag ratio to that of the plane diffuser.
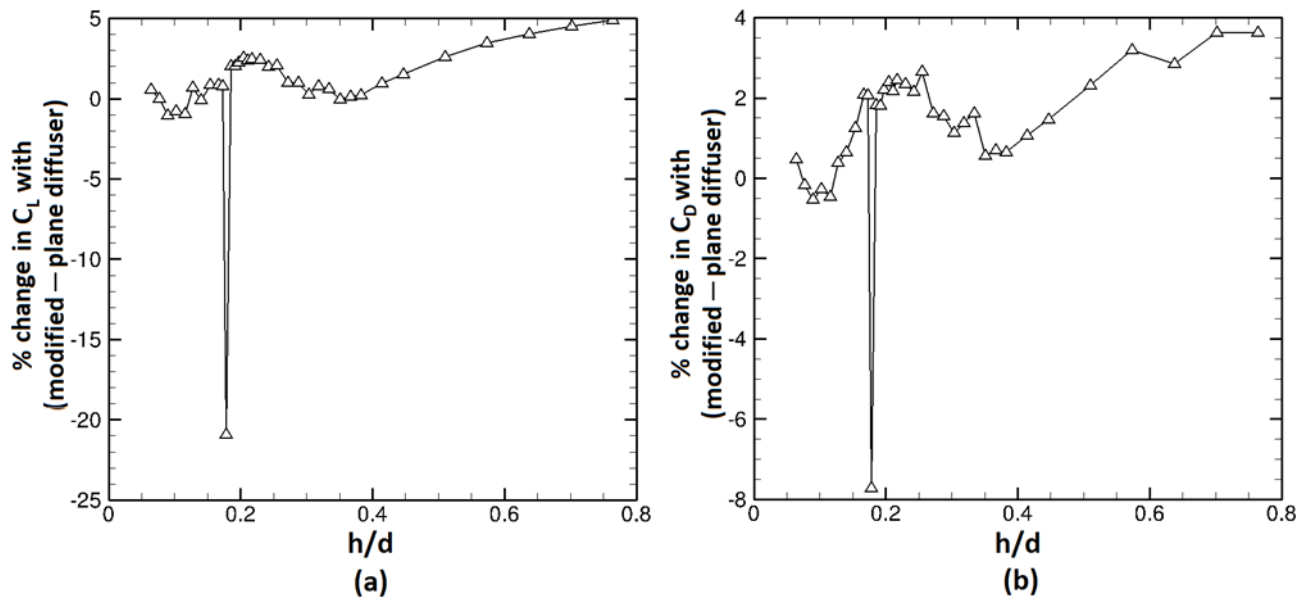

Fig. 5: Percentage difference in force coefficients between the modified and plane diffusers across the range of ride heights ($h/d = 0.764$ to 0.064) investigated for: **(a)** C_L ; **(b)** C_D
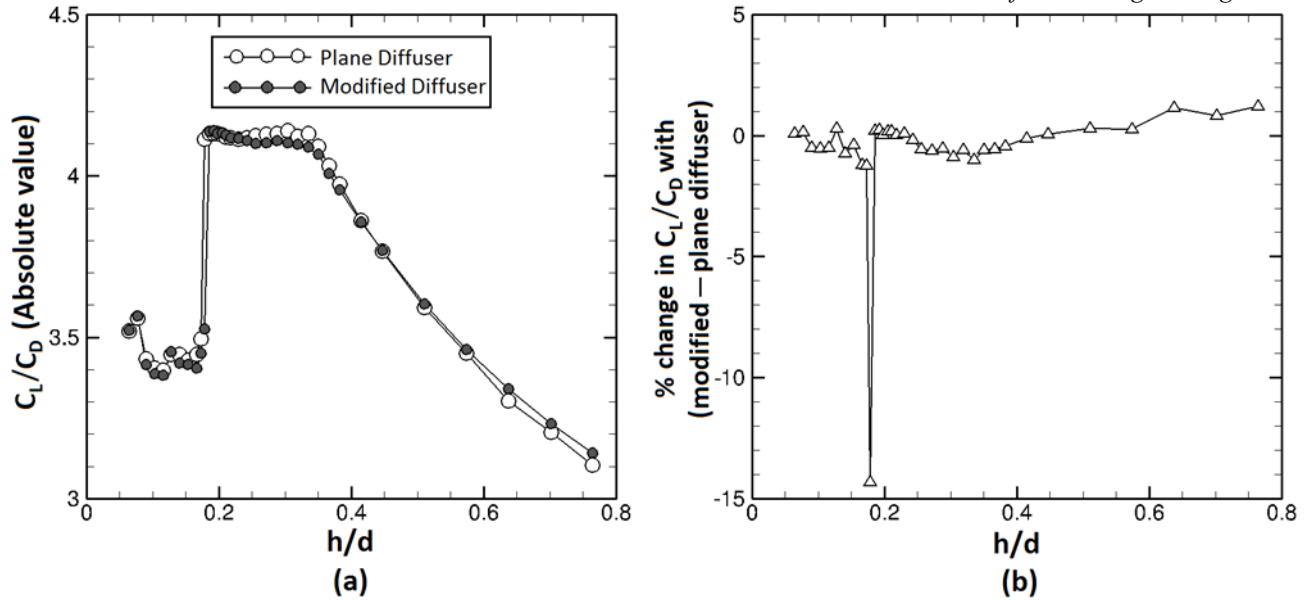
Fig. 6: (a) Lift-to-drag ratio measured across the range of ride heights ($h/d = 0.764 \; to \; 0.064$) investigated for the plane and modified diffusers; **(b)** Percentage difference in lift-to-drag ratio between the modified and plane diffusers across the range of ride heights investigated

3.2   Surface Pressure Distribution Analysis

The centerline and spanwise surface pressures across the flat underbody and diffuser ramp of the bluff body provided further insight into the behavior of the underbody flow passing through the diffuser channel at various ride heights. The underbody centerline and spanwise pressure distributions for both the plane diffuser and the modified diffuser are shown in Figures 7 and 8. The pressure distributions are presented for ride heights $h/d = 0.764, \; 0.382, \; 0.191, 0.153,$ and 0.064. As highlighted in the force curves of Figure 4, flow regime 'A' is represented by $h/d = 0.764 \; and \; 0.382$ while flow regimes 'B', 'C' and 'D' are represented by $h \; /d = 0.191, 0.153,$ and 0.064 respectively.

Each ride height we tested indicated that the velocity of the underbody flow dictated the static pressure behavior underneath the diffuser bluff body. The curvature at the start of the underbody induced a flow curvature effect which causes an increase in flow velocity at the curved underbody nose section hence the suction peak as a result of the radial pressure gradient at the start of the flat section. Downstream of that location, pressure recovery occurred briefly due to a reduction in the flow velocity effect from the start of the flat section. However, beyond the brief pressure recovery, static pressure reduced gradually due to the interaction of the diffuser exit on the inlet as a result of the pressure recovery between both points (diffuser pump-down effect). This leads to the peak velocity at the diffuser inlet producing a corresponding peak suction at the same location. The subsequent pressure recovery downstream of the diffuser inlet involved an

adverse pressure gradient, with the consequent possibility of flow separation. The C_p plots[2] of Figure 7 also indicate that peak suction at the diffuser inlet increased from that of the force-enhancement ride height ($h/d = 0.764$, Fig. 7a) to the maximum-force ride height ($h/d = 0.191$, Fig. 7c), subsequently declining with further height reduction.

The underbody surface pressures and diffuser inlet peak suction for both diffusers were identical. The magnitude of the diffuser inlet peak appeared to determine the underbody static pressures upstream of the diffuser inlet, with increasing suction recorded as the ride height was reduced from $h/d = 0.764$ to 0.191. The increase in downforce achieved by the modified diffuser across the range of ride heights was caused by the second pressure-recovery regime, where the convex bump is located. The suction induced by the bump as shown in Figure 7 lowers the static pressure in the area where the bump is located.

The spanwise surface pressure distributions across the diffuser ramp (Figure 8) suggest that the flow behavior through the diffuser is symmetric about the centerline at $h/d = 0.764, 0.382$ and 0.191 but asymmetric at $h/d = 0.153$ and 0.064. The symmetric and asymmetric flow also signified the presence of a distinct flow behavior along the lateral sides of the diffuser.

As shown in Figure 8a ($h/d = 0.764$), the transverse pressure distributions gradually flatten further downstream. In Figure 8b ($h/d = 0.382$), the pressure distributions for the plane and modified diffusers were identical at $x/d = 3.63$, but by $x/d = 6.29$ the pressure distribution for the modified diffuser was lower than that of the plane diffuser, reflecting the enhanced suction induced by the bump. This situation continued to the maximum downforce condition (Figure 8c) but disappeared when the ride height entered the low force regime (D). At the lower ride heights (Figures 8d and 8e) there was a notable asymmetry in the spanwise pressure distribution. This will be discussed further in the next section.

---

[2] Throughout this paper, $-C_p$ represents suction (sub-atmospheric pressures).
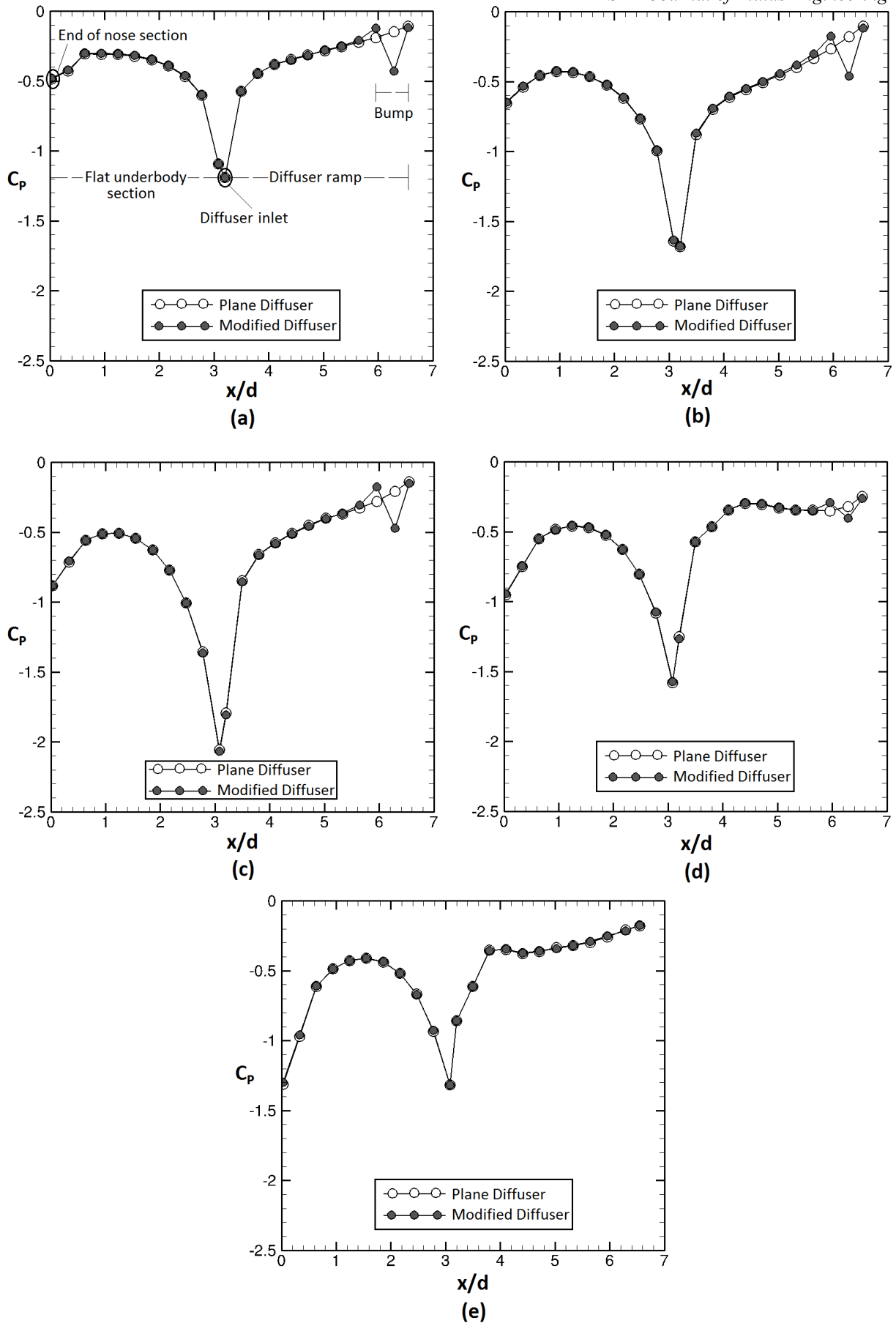
Fig. 7: Centerline surface pressure distribution at **(a)** $h/d = 0.764$ **(b)** $h/d = 0.382$ (both within the force-enhancement regime); **(c)** $h/d = 0.191$(within the maximum-force regime); **(d)** $h/d = 0.153$ (within the force-reduction regime); **(e)** $h/d = 0.064$ (within the low-force regime).

13

Fig. 8: Spanwise surface pressure distribution at **(a)** $h/d = 0.764$ for all x/d locations of the plane diffuser **(b)** $h/d = 0.382$ (both within the force-enhancement regime); **(c)** $h/d = 0.191$(within the maximum-force regime); **(d)** $h/d = 0.153$ (within the force-reduction regime); **(e)** $h/d = 0.064$ (within the low-force regime).
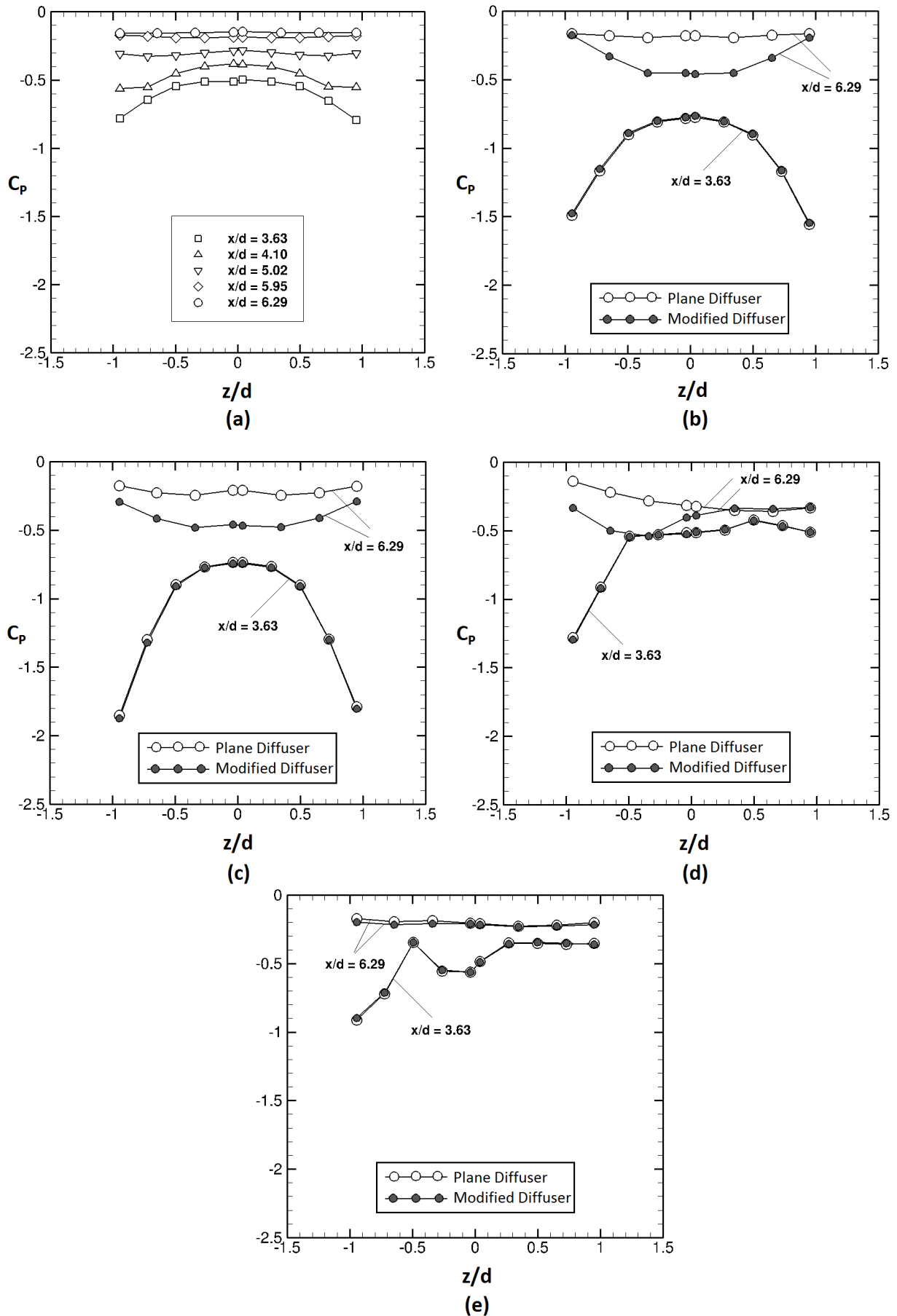
3.3 Surface Flow Visualization Analysis

Flow visualization on the surface of the diffuser ramp provided further information about the flow features of the diffuser. As shown in Figures 9 to 12, the surface flow features were distinct for ride heights ($h/d = 0.764$ and $0.382; 0.191; 0.153; 0.064$) representing the four force regimes. However, there were also differences in the surface flow features of the modified diffuser at the location of the bump, which further explains its improved aerodynamic performance relative to the baseline diffuser.

The surface flow features in the force-enhancement flow regime ($h/d = 0.764$ and 0.382) indicated the presence of longitudinal vortices (curved pathlines) along the sides of the diffuser ramp (Fig. 9). The existence of this vortex pair confirmed the results of previous studies [5, 9, 11, 12] in which the longitudinal vortices originating from either side of the diffuser inlet were propagated in the streamwise direction by the pressure difference along the diffuser. In addition, Figure 9 shows the diffuser flow symmetry about the centerline ($z/d = 0$). This explains the symmetric spanwise surface pressure distribution, with the suction peaks on each side corresponding to the longitudinal vortices. A short separation region appears across the span of the diffuser inlet, except for the sides where the longitudinal vortex pair originated. However, the vortex pair appeared to travel downstream towards the center of the diffuser ramp indicating a separation from the diffuser end-plates. Also, the diffusion of the curved pathlines at the latter part of the diffuser surface — towards the diffuser exit — indicated the weakening of the vortex pair and detachment from the diffuser surface. When the ride height was reduced from $h/d = 0.764$ to 0.382, the curved lines became more apparent and appeared to extend further downstream. This indicates an enhancement in vortex strength (vorticity) due to the increase in diffuser inlet velocity which in turn translates to increased downforce.

At $h/d = 0.764$ (Fig. 9a) for the modified diffuser, there was a small recirculation region at each side where the bump merges with the end-plates. However, the flow over the bump appeared mostly attached, except for a region along each side of the bump close to the edge of the diffuser exit. Along those regions, the weakened vortex was detached from the diffuser surface and replaced by flow recirculation. At $h/d = 0.382$ (Fig. 9b), the recirculation region on each side close to where the bump meets the plane diffuser ramp was more pronounced due to the greater

vortex strength. However, the flow over the bump was increasingly attached to the bump, except along the sides of the bump where recirculation was more distinct.
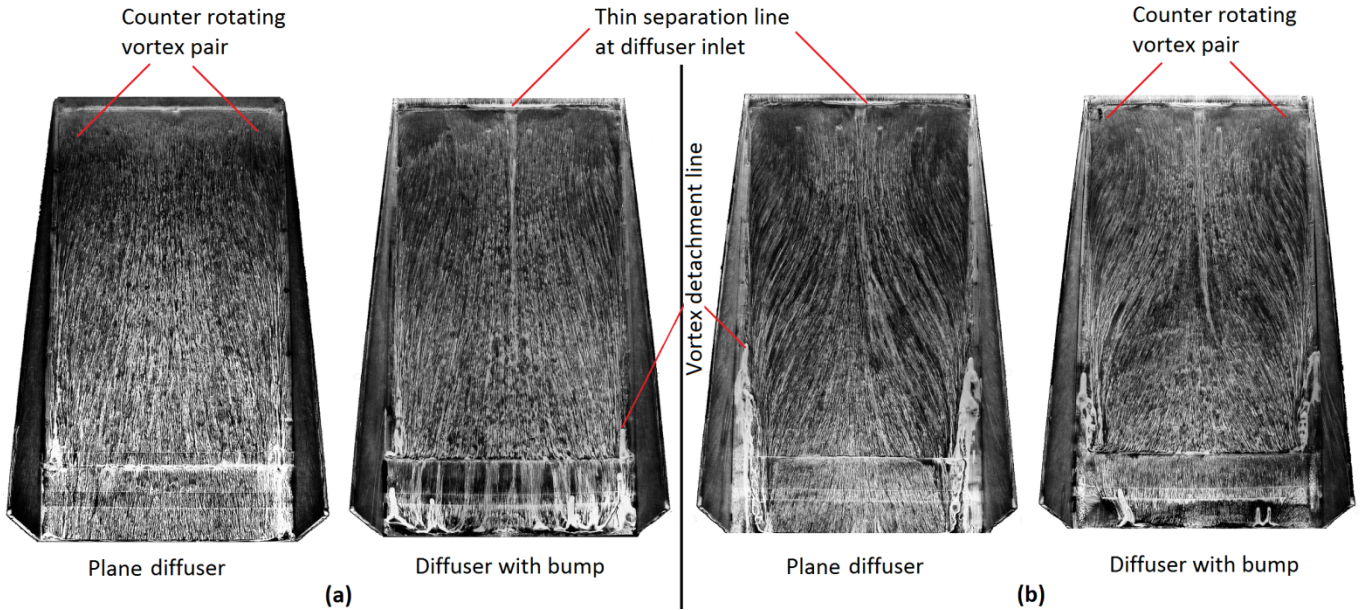

Fig. 9: Surface flow patterns at force-enhancement regime ride heights: (a) $h/d = 0.764$ (b) $h/d = 0.382$ (flow from top to bottom)

In the maximum-force flow regime ($h/d = 0.191$), there is an increased curvature of the surface flow pathlines and the separation line on each side of the diffuser ramp is present (Fig. 10). The dominance of the curved pathlines signifies a further increase in vortex strength and increased suction, as indicated by the spanwise pressure distribution. In addition, the flow remained symmetric but we observed a thickening of the thin separation line along the central region of the diffuser inlet (between $z/d = 0.25$ and -0.25). The separation bubble extended further down the central region to a distance about two-thirds of the diffuser length. This indicated that the constrained underbody flow entering the diffuser had a greater velocity and that the adverse pressure gradient encountered by the diffuser flow had increased. At the bottom half of the diffuser ramp towards the diffuser exit, the diminished appearance of the curved flow pathlines of the vortex pair along the sides of the diffuser indicated detachment from the diffuser surface. However, the declining presence of the separation bubble towards the diffuser exit indicated that the flow had reattached to the diffuser surface.
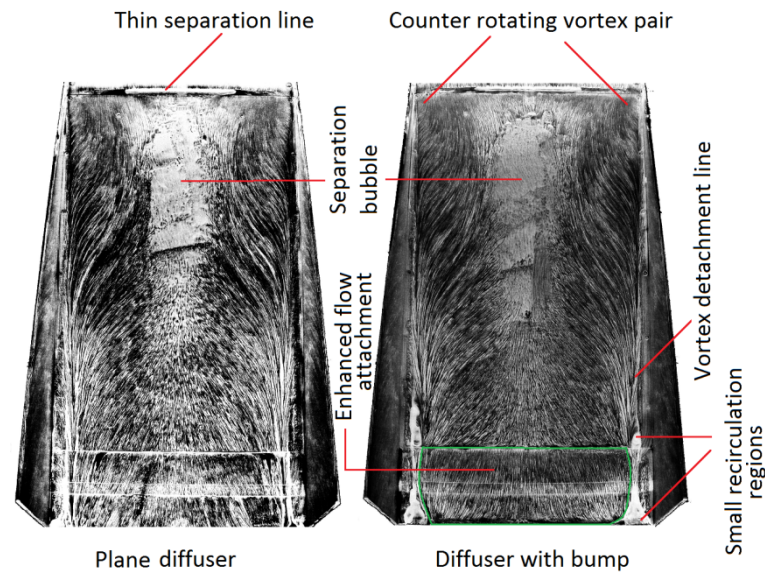
Fig. 10: Surface flow patterns at the ride height of $h/d = 0.191$ in the maximum-force regime (flow from top to bottom)

On the surface of the bump of the modified diffuser, the flow appeared to be largely attached. However, the recirculation regions on each side of the bump remained visible and appeared close to the edge of the diffuser exit. The undisturbed flow pathlines for both diffusers at the site corresponding to the position of the bump indicated that the flow was attached. Flow attachment was more prevalent around the central area of the bump relative to the same location of the plane diffuser. Notably, surface pressures measured at $x/d = 6.29$ (Fig. 8c) indicated that the lower pressures are present on the central area of the bump thus indicating relatively high flow velocity at that region.

At the force-reduction ride height ($h/d = 0.153$), the asymmetric flow features in Figure 11 confirmed the asymmetric surface pressure distribution. Only one of the longitudinal edge vortices remained, and the non-existing vortex was replaced by a diagonal flow that appeared to travel towards the existing vortex. Part of the diagonal flow appeared to have reversed towards the diffuser inlet and the other portion of the diagonal flow appeared to have reversed around a significant area of one side of the diffuser. However, along the longitudinal edge of the surviving vortex, the flow appeared to have largely detached from the diffuser end plate. In addition, across the span of the diffuser inlet, the thin separation line appeared to have moved towards the side featuring the surviving vortex. This implies that the surviving vortex is weaker than the same vortex at the maximum-force ride height (as confirmed by pressure measurements). The asymmetry of the diffuser flow at the force-reduction ride height was previously reported to be

random, and the vortex bursting phenomenon switched from one vortex to the other [9-11]. Furthermore, the asymmetry was reported [9] possibly to have been induced by an error introduced when aligning the model to a zero-yaw angle, or imperfections in the test model underbody surface, as postulated in missile and slender body aerodynamics [29]. However, repeated tests and marginal yaw adjustments in this present study did not restore flow symmetry.
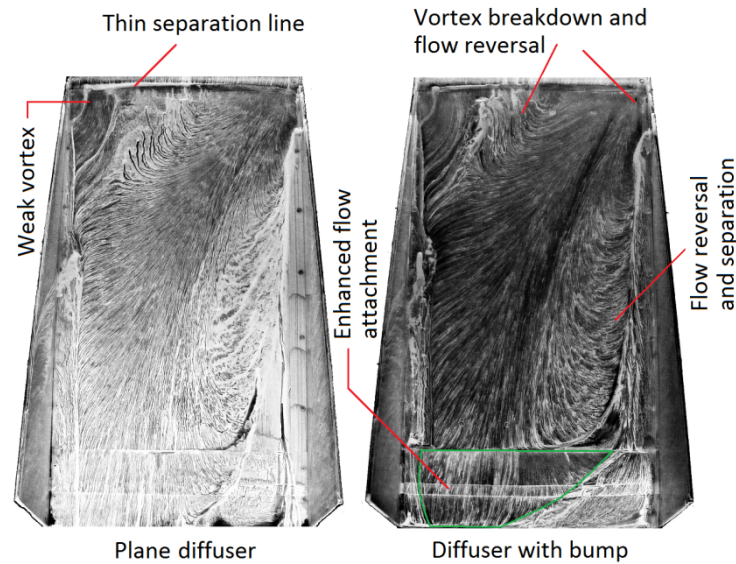

Fig. 11: Surface flow patterns at the ride height of $h/d = 0.153$ in the force-reduction regime (flow from top to bottom)

At the force-reduction ride height, the constrained underbody 3D flow is further constrained if the flat underbody and moving ground condition turbulent boundary layer thicknesses are each assumed to be the same as that of a flat plate ($\sim 10.5\ mm$ based on a zero-pressure-gradient flat-plate approximation). This could mean that the decrease in the diffuser inlet area as a result of the reduction of ride height below the critical ride height ($h/d = 0.191$) may have induced a thickening of the retarding boundary layer flow. Hence, the dominant flow separation, reversal of the diffuser flow and vortex breakdown (accompanied by downforce loss) may be the consequence of the reduced diffuser inlet area. In the case of the modified diffuser, the flow patterns remained broadly similar but the attachment of the flow on about half of the bump's surface area, particularly on the side featuring the surviving vortex appeared to have generated more suction. This was supported by the lower surface pressures ($x/d = 6.29$) on this half of the modified diffuser compared to the corresponding half of the plane diffuser (Figure 8d). As a result, the modified diffuser generated more downforce than the baseline diffuser.
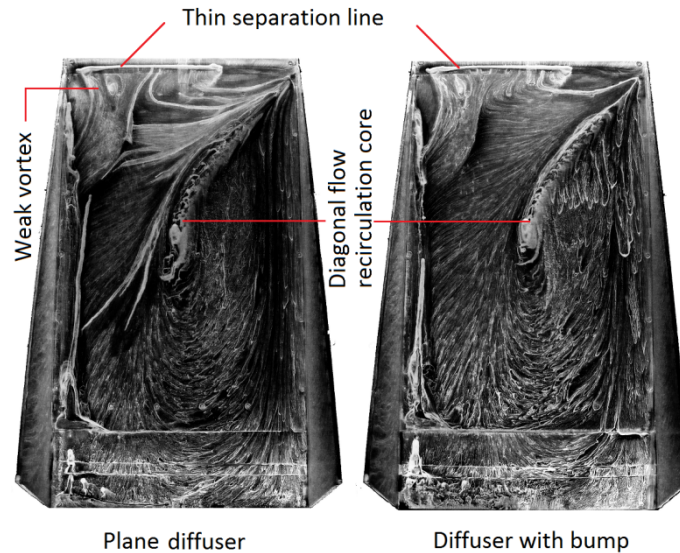
Fig. 12: Surface flow patterns at the ride height of $h/d = 0.064$ in the low-force regime (flow from top to bottom)

The low-force flow regime was delineated by the flow patterns at a ride height of $h/d = 0.064$ (Figure 12). The features of this flow regime indicated that although the weakened solitary vortex still existed, the flow was almost fully dominated by flow separation and flow reversal. This was highlighted by the center of the recirculation, which appeared more pronounced and stretched diagonally across the diffuser ramp surface. In addition, the detachment of the existing vortex flow from the end plate began close to the diffuser inlet. The thin sliver of the separation line at the diffuser inlet also stretched to cover ~70% of the diffuser inlet span. This implies that the underbody flow is largely a boundary layer flow, which is subjected to a strong adverse pressure gradient. The low downforce generated at this ride height was supported by the substantial increase in surface pressures (low suction) in the diffuser centerline and spanwise pressure distributions. The modified diffuser generated only ~0.56% more downforce $(-C_L)$ than the baseline diffuser because the flow on one-third of the bump surface area (on the side of the surviving vortex) was still attached.

3.4   Diffuser Inlet Boundary Layer Profiles

Velocity profiles (U/U_∞) of the boundary layer were measured at the diffuser inlet $(x/d = 3.14)$. As shown in Figure 13, the boundary layer velocity profiles were recorded on the diffuser centreline $(z/d = 0)$ and at $h/d = 0.382; 0.191; 0.153;$ and 0.064 representing the four force regimes 'A' to 'D'.
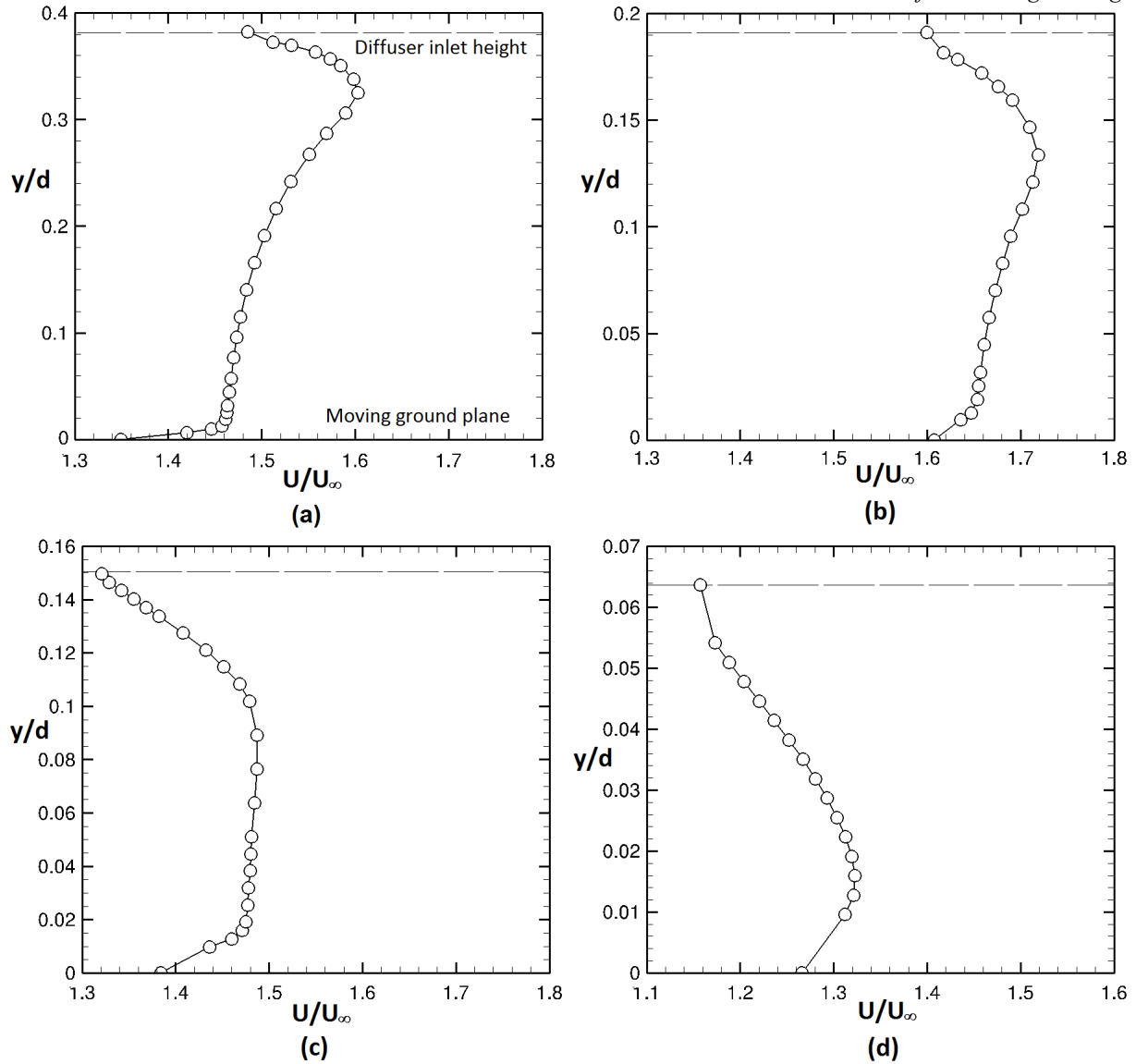
Fig. 13: Boundary layer velocity profiles at diffuser inlet ($x/d = 3.14$) centre point ($z/d = 0$) for: **(a)** $h/d = 0.382$; **(b)** $h/d = 0.191$; **(c)** $h/d = 0.153$ and **(d)** $h/d = 0.064$

The velocity gradients at the top and bottom of the velocity profiles, as shown in Figure 13, indicate the presence of boundary layer development on the diffuser inlet and on the moving ground. There is a small boundary layer on the ground due to the higher freestream velocity under the vehicle. Over the height range encompassing regimes 'A' to 'C' the boundary layers on the underbody and the ground are clearly separate. At the lowest ride height (Regime 'D') the two boundary layers appear to merge and the peak velocity has started to reduce.

Boundary layer removal upstream of the moving ground plane eliminates the residual boundary layer from the wind tunnel to simulate a moving vehicle over stationary ground, however, a boundary layer develops on the ground plane because of the flow acceleration under the body. This only interacts with the boundary layer on the underbody at the lowest ride height tested.

4. DISCUSSION

The surface flow visualization combined with the force and surface pressure measurements indicated that the complex flow physics of the diffuser has a significant aerodynamic impact. Across a wide range of ride heights, the diffuser was characterized by different flow characteristics which determined its aerodynamic performance. Notably, two major flow characteristics determine which of four flow regimes is prevalent: the peak suction at the diffuser inlet and the longitudinal vortices along both sides of the diffuser.

Under the force-enhancement flow regime, the longitudinal vortex pair is formed when peak suction is established at the diffuser inlet fed by the diffuser pumping effect at the inlet [6-14]. The underbody centerline pressures we recorded indicate that the intensity of the inlet suction increased with decreasing ride height until we reached the maximum downforce ride height. Likewise, spanwise surface pressures and flow visualization indicated a similar increase in suction along both sides of the diffuser due to an increase in vortex strength. However, another flow characteristic that should be highlighted is the increasing adverse pressure gradient encountered by the flow as the ride height is reduced. This was responsible for the detachment of the flow (including its vortical components) from the surface of the diffuser.

The flow physics observed under the force-reduction and low-force flow regimes were the antithesis of those observed under the force-enhancement and maximum-force flow regimes. The diffuser flow under the force-reduction and low-force flow regimes was asymmetric, as defined by the decrease in inlet peak suction and the complete breakdown of one of the longitudinal vortices. In addition, flow separation at the diffuser inlet and downstream flow recirculation were prevalent in force-reduction and low-force flow regimes. However, as observed under the force-enhancement to the maximum-force regimes, the intensity of the flow characteristics increased when the ride height was reduced from the force-reduction to the low-force regime values.

One phenomenon that requires further investigation is the basis for the selection of one of the two longitudinal vortices for vortex breakdown. The boundary layer thickness at the force-reduction and low-force ride heights occupy a greater volume of the underbody flow entering the diffuser, indicating that the boundary layer-dominated flow is at least partly influencing the flow asymmetry associated with the force-reduction and low-force flow regimes. Even so, the size of the boundary layer as estimated by Senior et al. [9-11] was smaller than the ride height at which the onset of flow asymmetry was observed, so the bistability of the asymmetric flow cannot be

fully explained by the retardation of the boundary layer flow. Notably, the spanwise surface pressure distributions for the maximum downforce regime indicate that one of the vortices of the pair generated suction that was ~3.4% greater than the other vortex, despite the general symmetry of the diffuser flow. Thus, it can be surmised that early indications of flow asymmetry may have begun at the maximum downforce ride height. Also, the stronger vortex appeared to be the surviving vortex in the force-reduction and low-force regimes, as previously reported [9, 11]. The vortex strength (vorticity) for each vortex of the longitudinal pair in the maximum-force flow regime may, therefore, determine which vortex survives in the force-reduction and low-force regimes. The flow visualization for the force-reduction and low-force regimes indicated that the stronger vortex appeared also to have pulled flow from the other side of the diffuser where vortex bursting occurred (hence the diagonal flow pathlines).

The bump on the modified diffuser ramp surface appeared to be the only source of additional downforce compared to the plane diffuser. The lower surface pressures on the bump suggested that the flow velocity on the bump has increased. This occurrence can only be explained by flow curvature effect; where the curvature of the convex bump introduces a shape into the airflow, which curves the streamlines and causes the flow to accelerate. As a result of this action, a radial pressure gradient is generated along the length of the bump and the detachment of the flow from the diffuser ramp towards the exit is replaced by flow attachment due to flow entrainment onto the bump surface. Hence, the second static pressure drop and pressure-recovery region downstream of the diffuser inlet is created reducing the average pressure close to the diffuser exit, which, in turn, led to the increase in downforce $(4.9\%, 0.73\%, 2.03, 0.84\%,$ and $0.56\%)$ for the ride heights presented $(h/d = 0.764, 0.382, 0.191, 0.153$ and 0.064 respectively$)$.

Also, as with any lifting surface, the lift force generated comes with a drag force. For the ride heights presented $(h/d = 0.764, 0.382, 0.191, 0.153,$ and $0.064)$, the additional downforce generated by the convex bump induced an additional aerodynamic drag $(\text{in terms } of \ C_D : \ + 0.01,$ $+0.005, +0.009, +0.001,$ and $+ 0.002$ respectively$)$. The additional drag is due to the profile drag created by the convex surface. However, the marginal increase in drag may have been kept low by the low skin friction of the attached flow on the bump. Another attribute of the convex bump worth noting is its geometric parameters. It was observed through computational fluid dynamics investigations [21] that the length and thickness of the bump dictates the additional downforce and drag levels. An increase in bump length will increase downforce, however, an increase in the

bump's thickness will increase downforce up to a point after which further increase in thickness will reduce the lift-to-drag ratio of the bump as a result of increased profile drag. This is because the curvature has become too steep (inducing a significant adverse pressure gradient) for the flow to remain attached to the bump surface. Thus, optimal bump thickness was discovered to be within 25% to 30% of the diffuser ramp boundary layer thickness. In addition, to prevent a disruption of the static pressure peak at the diffuser inlet and to enable optimal aerodynamic performance of the second-stage pressure recovery region in delaying pressure recovery to freestream at the diffuser exit, it was discovered that the length of the bump should be approximately 25% of the diffuser ramp length.

5.   CONCLUSION

We have compared the 3D flow physics of a plane-surface diffuser ramp (baseline diffuser) and another with a convex bump (modified diffuser) to determine the basis of the increased downforce generated by the induction of a secondary pressure-recovery region. Our data confirmed the following flow regime characteristics described in previous studies:

- The force-enhancement flow regime is a symmetric flow comprising a pair of counter-rotating streamwise vortices along the sides of the diffuser. The vortices spread inwards as they grow downstream due to the pressure difference between the inside and outside of the diffuser. Downstream of the diffuser inlet, the adverse pressure gradient causes the vortices to diffuse and detach from the diffuser ramp.

- The maximum-force flow regime is also a symmetric flow with a more pronounced appearance of the flow features described for the force-enhancement flow regime. The longitudinal vortex pair is stronger and the flow encounters a greater adverse pressure gradient. This creates a separation bubble around the center of the diffuser ramp originating at the diffuser inlet and stretching towards the mid length of the diffuser. However, the flow reattaches downstream with the vortices appearing diffused and detached from the diffuser ramp.

- In the force-reduction flow regime, the flow is asymmetric with a complete bursting of one of the vortex pair. The flow entering the diffuser is a boundary-layer dominant flow, hence flow separation at the diffuser inlet is enhanced and reverse flow is induced downstream. Downforce reduction is the ultimate consequence of this asymmetric flow.

- The low-force flow regime can be aptly described as an enhancement of the flow features of the force-reduction flow regime. The boundary layer flow entering the diffuser almost entirely separates from the diffuser inlet. Also, the scale of flow recirculation is increased with its core stretching diagonally across the diffuser. Although the surviving vortex is still present, it is much weaker and as a result the downforce generated is low.

- The convex bump was found largely to increase downforce to a high of 4.9% at the highest ride height of the force-enhancement regime and 2.03% at the diffuser maximum downforce ride height, however, percentage downforce increment gradually reduced with decreasing ride height.

- It was also discovered that the bump did not delay the emergence of the type 'C' flow regime (force-reduction) as ride height was reduced because it had no control over the vortex breakdown at the diffuser inlet associated with the type 'C' flow regime.

The flow features were similar in both diffusers but the convex bump enhances the aerodynamic performance of the diffuser by enhancing streamwise flow velocity and generating a radial pressure gradient with the application of flow curvature. This reflects the increased flow attachment induced by the bump close to the diffuser exit. As result, the surface of the bump generates additional suction through a second pressure-recovery region close to the diffuser exit, thus increasing the downforce.

ACKNOWLEDGMENTS

Nomenclature

A = bluff body frontal area (m^2)

C_D = drag coefficient $\dfrac{D}{q_\infty A}$

C_L = lift coefficient $\dfrac{L}{q_\infty A}$

C_p = pressure coefficient $\dfrac{p - p_\infty}{q_\infty}$

d = diffuser half-width (m)

D = aerodynamic drag (N)

h = bluff-body ride height (m)

h_0 =   diffuser height (m)

H =   bluff-body height (m)

L =   aerodynamic lift (N) (positive upwards)

L_B =   bluff-body length (m)

L_D =   diffuser length (m)

p =   static pressure (Pa)

p_∞ =   freestream pressure (Pa)

q_∞ =   freestream dynamic pressure (Pa), $\frac{\rho U_\infty^2}{2}$

Re =   Reynolds number based on bluff-body length $\frac{U_\infty L_B}{\nu}$

u, v, w =   velocity components in x, y, z directions

U =   total velocity $\sqrt{u^2 + \mathrm{v}^2 + w^2}$, $(m\ s^{-1})$

U_∞ =   freestream velocity $(m\ s^{-1})$

W =   diffuser width (m)

x, y, z =   Cartesian coordinates from origin (see Fig. 2a): x is positive downstream, y is positive upwards, z is positive to port side

Greek Symbols

θ =   diffuser angle $(degrees)$

μ =   dynamic viscosity $(kg\ m^{-1}\ s^{-1})$

ν =   kinematic viscosity $(m^2\ s^{-1})$, $\left(\frac{\mu}{\rho}\right)$

ρ =   air density $(kg\ m^{-3})$

Abbreviations

CAD   =   computer aided design

CFD   =   computational fluid dynamics

IDDES   =   improved delayed detached eddy simulation

LES   =   large eddy simulation

PISO   =   pressure implicit with splitting of operator

RANS   =   Reynolds-averaged Navier-Stokes

SIMPLE   =   semi-implicit method for pressure linked equations

REFERENCES

[1] Katz, J., 2006, "Aerodynamics of the Complete Vehicle," *New Directions in Race Car Aerodynamics,* 2nd revised ed., Bentley Publishers, Cambridge, Massachusetts, pp. 221–222.

[2] Barnard, R. H., 2001, "Racing Cars and Other High-Performance Vehicles," *Road Vehicle Aerodynamic Design: An Introduction,* Mech Aero Publishing, St. Albans, UK, 2nd revised ed., pp. 161–164.

[3] Agathangelou, B. and Gascoyne, M., 1998, "Aerodynamic Design Considerations of a Formula 1 Racing Car," SAE Technical Paper 980399.

[4] Zhang, X., Toet, W., and Zerihan, J., 2006, "Ground Effect Aerodynamics of Racing Cars" Applied Mechanics Review, 59(1), pp. 33–49.

[5] George, A. R., 1981, "Aerodynamic Effects of Shape, Camber, Pitch on Ground-vehicle Bodies", ASME Journal of Fluids Engineering, 103(4), pp. 631–637.

[6] George, A. R. and Donis, J., 1983, "Flow Patterns, Pressures and Forces in the Underside of Idealised Ground Effect Vehicles", *Proceedings of the ASME Fluids Engineering Division Symposium on Aerodynamics of Transportation II,* 7, pp. 69–79.

[7] Cooper, K. R., Bertenyi, T., Dutil, G., Syms, J. and Sovran, G., 1998, "The Aerodynamic Performance of Automotive Underbody Diffusers," SAE Technical Paper 980030.

[8] Cooper, K. R., Sovran, G. and Syms, J., 2000, "Selecting Automotive Diffusers to Maximize Underbody Downforce," SAE Technical Paper 2000–01–0354.

[9] Senior, A. E. and Zhang, X., 2000, "An Experimental Study of a Diffuser in Ground Effect", American Institute of Aeronautics and Astronautics, Paper 2000–0118.

[10] Senior, A. E. and Zhang, X., 2000, "The Force and Pressure of a Diffuser-Equipped Bluff Body in Ground Effect," ASME Journal of Fluids Engineering, 123(1), pp. 105–111.

[11] Senior, A., 2002, "The Aerodynamics of a Diffuser Equipped Bluff Body in Ground Effect," Ph.D. Thesis, University of Southampton, UK.

[12] Ruhrmann, A. and Zhang, X., 2003, "Influence of Diffuser Angle on a Bluff Body in Ground Effect", ASME Journal of Fluids Engineering, 125(2), pp. 332–338.

[13] Jowsey, L. and Passmore, M., 2010, "Experimental Study of Multiple-Channel Automotive Underbody Diffusers", *Proceedings of the Institution of Mechanical Engineers, Part D: Journal of Automobile,* 224(7), pp. 865–879.

[14] Jowsey, L., 2013, "An Experimental Study of Automotive Underbody Diffusers", Ph.D. Thesis, Loughborough University, UK.

[15] Marklund, J., 2013, "Under-body and Diffuser Flows of Passenger Vehicles", Ph.D. Thesis, Chalmers University of Technology, Sweden.

[16] Puglisevich, L. S., 2013, "Large Eddy Simulation for Automotive Vortical Flows in Ground Effect", Ph.D. Thesis, Loughborough University, UK.

[17] Gad-el-Hak, M., 2000, *"Flow Control: Passive, Active, and Reactive Flow Management,"* Cambridge University Press, Cambridge, UK, pp. 112, 151–152, 163, 176.

[18] Garcia, D. L. and Katz, J., 2003, "Trapped Vortex in Ground Effect," AIAA Journal, 41(4), pp. 674–678.

[19] Katz, J. and Morey, F., 2008, "Aerodynamics of Large-Scale Vortex Generator in Ground Effect," ASME Journal of Fluids Engineering, 130(7), Paper No. 071101.

[20] Kuya, Y., Takeda, K., Zhang, X., Beeton, S. and Pandaleon, T., 2009, "Flow Separation Control on a Race Car Wing with Vortex Generators in Ground Effect," ASME Journal of Fluids Engineering, 131(12), Paper No. 121102.

[21] Ehirim, O. H., 2017, "Aerodynamics and Performance Enhancement of the Ground Effect Diffuser", PhD Thesis, Cranfield University, Shrivenham, UK.

[22] Gibson, M. M., Verriopoulos, C. A. and Vlachos, N. S., 1984, "Turbulent Boundary Layer on a Mildly Curved Convex Surface Part 1: Mean Flow and Turbulence Measurements," Experiments in Fluids, 2(1), pp. 17–24.

[23] Muck, K. C., Hoffmann, P. H. and Bradshaw, P., 1985, "The Effect of Convex Surface Curvature on Turbulent Boundary Layers," Journal of Fluid Mechanics, 161, pp. 347–369.

[24] So, M. C. R. and Mellor, G. L., 1973, "Experiment on Convex Curvature Effects in Turbulent Boundary Layers," Journal of Fluid Mechanics, 60(1), pp. 43–62.

[25] Bradshaw, P., 1973, *"Effects of Streamline Curvature on Turbulent Flow,"* AGARDograph AG-169.

[26] Knowles, K. and Finnis, M. V., 1998, "Development of a New Open-Jet Wind Tunnel and Rolling Road Facility" *In: 2nd MIRA International Conference on Vehicle Aerodynamics,* Coventry, UK.

[27] Abernethy, R. B., Benedict, R. P., and Dowdell, R. B., 1985, "ASME Measurement Uncertainty," ASME Journal of Fluids Engineering, 107(2), pp. 161–164.

[28] Moffat, R. J., 1988, "Describing the Uncertainties in Experimental Results," Experimental Thermal and Fluid Science. 1(1), pp 3–17.

[29] Dexter, P. C., 1982, "An Experimental Investigation of the Aerodynamics of Slender Axisymmetric Bodies at High Angles of Incidence", PhD Thesis, University of Bristol, UK.